

Soft X-ray harmonic comb from relativistic electron spikes

A. S. Pirozhkov,¹ M. Kando,¹ T. Zh. Esirkepov,¹ P. Gallegos,^{2,3} H. Ahmed,⁴ E. N. Ragozin,⁵ A. Ya. Faenov,^{1,6} T. A. Pikuz,^{1,6} T. Kawachi,¹ A. Sagisaka,¹ J. K. Koga,¹ M. Coury,³ J. Green,² P. Foster,² C. Brenner,^{2,3} B. Dromey,⁴ D. R. Symes,² M. Mori,¹ K. Kawase,¹ T. Kameshima,¹ Y. Fukuda,¹ L. Chen,¹ I. Daito,¹ K. Ogura,¹ Y. Hayashi,¹ H. Kotaki,¹ H. Kiriya,¹ H. Okada,¹ N. Nishimori,⁷ T. Imazono,¹ K. Kondo,¹ T. Kimura,¹ T. Tajima,¹ H. Daido,¹ P. Rajeev,² P. McKenna,³ M. Borghesi,⁴ D. Neely,^{2,3} Y. Kato,¹ and S. V. Bulanov^{1,8}

¹Advanced Beam Technology Division, JAEA, 8-1-7 Umemidai, Kizugawa, Kyoto 619-0215, Japan

²Central Laser Facility, Rutherford Appleton Laboratory, STFC, Chilton, Didcot, Oxon OX11 0QX, UK

³University of Strathclyde, Department of Physics, SUPA, Glasgow G4 0NG, UK

⁴Centre for Plasma Physics, The Queen's University of Belfast, Belfast BT7 1NN (UK)

⁵P. N. Lebedev Physical Institute, RAS, Leninsky prospekt 53, Moscow 119991, Russia

⁶Joint Institute of High Temperatures, RAS, Izhorskaja st. 13/19, Moscow 127412, Russia

⁷Laser Application Technology Division, JAEA, 2-4 Shirakata-Shirane, Tokai, Ibaraki 319-1195, Japan

⁸A. M. Prokhorov Institute of General Physics, RAS, Vavilov st. 38, Moscow 119991, Russia

(Dated: April 20, 2022)

We demonstrate a new high-order harmonic generation mechanism reaching the ‘water window’ spectral region in experiments with multi-terawatt femtosecond lasers irradiating gas jets. A few hundred harmonic orders are resolved, giving $\mu\text{J}/\text{sr}$ pulses. Harmonics are collectively emitted by an oscillating electron spike formed at the joint of the boundaries of a cavity and bow wave created by a relativistically self-focusing laser in underdense plasma. The spike sharpness and stability are explained by catastrophe theory. The mechanism is corroborated by particle-in-cell simulations.

PACS numbers: 52.27.Ny, 42.65.Ky, 52.59.Ye, 52.35.Mw, 42.65.Re, 52.38.Ph

High-order harmonic generation, one of the most fundamental effects of nonlinear wave physics, originates from many nonlinearities, e.g. relativistic [1, 2] and ionizing matter effects [3]. Harmonics reaching the X-ray spectral region enable nanometer and attosecond resolution in biology, medicine, physics, and their applications. Several compact laser-based X-ray sources have been implemented, including plasma-based X-ray lasers [4], atomic harmonics in gases [3], nonlinear Thomson scattering [5] from plasma electrons [6, 7] and electron beams [8], betatron radiation [9], relativistic flying mirrors [10], and harmonics from solid targets [1, 2, 11] and electro-optic shocks [12]. Many of them [1, 5–11] come from relativistic laser-matter interactions, determined by the dimensionless laser pulse amplitude $a_0 = eE_0/m_e c\omega_0 > 1$ related to the laser peak irradiance by $I_{0L} = I_{\text{rel}} a_0^2 (\mu\text{m}/\lambda_0)^2$ for linear and $I_{0C} = 2I_{0L}$ for circular polarization. Here, e and m_e are the electron charge and mass, c is the speed of light in vacuum, ω_0 , λ_0 and E_0 are the laser angular frequency, wavelength and peak electric field, respectively, and $I_{\text{rel}} = 1.37 \times 10^{18} \text{W}/\text{cm}^2$ [2].

In this Letter we experimentally demonstrate bright Extreme Ultraviolet (XUV) and soft X-ray harmonics resolved up to a few hundred orders from gas jets irradiated by multi-terawatt femtosecond lasers. We propose a new mechanism of high-order harmonics generation.

We have performed two experimental campaigns using J-KAREN [13] and Astra Gemini [14] lasers. The laser pulse power P_0 , duration τ , wavelength λ_0 , off-axis parabolic mirror f-number, and irradiance in vacuum are

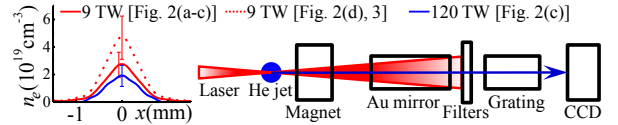


FIG. 1. (Color online) The experiment scheme (right) and He plasma density profile (left) for the shots in Figs. 2, 3.

9 TW, 27 fs, 820 nm, $f/9$, and $4 \times 10^{18} \text{W}/\text{cm}^2$ in the first campaign, and 120 TW, 54 fs, 804 nm, $f/20$, and $4 \times 10^{18} \text{W}/\text{cm}^2$ in the second campaign, respectively. Focusing laser pulses onto a supersonic helium gas jet, Fig. 1, we record harmonics in the 80–360 eV spectral region in the forward (laser propagation) direction, Figs. 2, 3. We use flat-field spectrographs [15], comprising a gold-coated grazing-incidence collecting mirror, spherical varied-linespace grating, and back-illuminated Charge Coupling Device (CCD), shielded by optical blocking filters – two $0.16 \mu\text{m}$ multilayer Mo/C, two $0.2 \mu\text{m}$ Pd, or one $0.2 \mu\text{m}$ Ag on $0.1 \mu\text{m}$ CH substrate. The acceptance angle is 3×10^{-5} sr in the first and 3×10^{-6} sr in the second campaign. In the latter case, the spectrograph has two channels for observation at 0° (forward direction) and 0.53° in the laser (linear) polarization plane. The wavelength calibration is performed in-place using spectra of Ar and Ne plasmas. The harmonics energy and photon numbers are conservatively estimated using idealized spectrograph throughputs, i.e. the products of the calculated [16] collecting mirror reflectivities and filter transmissions, measured diffraction grating efficiencies, and manufacturer-provided CCD efficiencies.

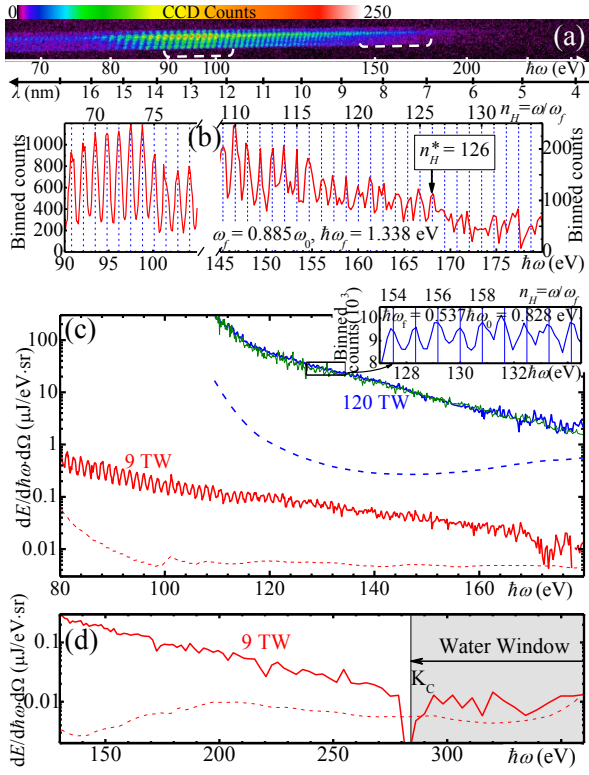


FIG. 2. (Color) Typical single-shot comb-like spectra. (a) Raw data for $P_0 = 9$ TW, $n_e = 2.7 \times 10^{19} \text{ cm}^{-3}$. (b) Lineouts for two regions marked in (a) by dashed brackets. Dotted vertical lines for harmonics of the base frequency $\omega_f = 0.885\omega_0$. The highest resolved order is $n_H^* = 126$. (c) Spectra for the shot shown in (a) (red) and for $P_0 = 120$ TW, $n_e = 1.9 \times 10^{19} \text{ cm}^{-3}$ obtained from the 2nd (blue) and 3rd (green) diffraction orders. Inset: harmonics in the 2nd diffraction order; similarly for the 3rd order. (d) The spectral region embracing the ‘water window’ for $P_0 = 9$ TW, $n_e = 4.7 \times 10^{19} \text{ cm}^{-3}$. The drop at the carbon K absorption edge, K_C , is due to hydrocarbon contamination. Dashed curves in (c,d) for background due to the CCD dark current, read-out noise, and scattered photons.

In both campaigns the laser power significantly exceeds the relativistic self-focusing threshold, $P_{\text{sf}} \approx 17 \text{ GW} \times (n_{\text{cr}}/n_e)$, where $n_{\text{cr}} = m\omega_0^2/4\pi e^2 \approx 1.1 \times 10^{21} \text{ cm}^{-3} (\mu\text{m}/\lambda_0)^2$ is critical density. Thus both lasers’ pulses self-focus to tighter spots reaching higher irradiance determined by the plasma density and laser power.

The comb-like spectra comprising even and odd harmonic orders of similar intensity and shape are generated by both linearly and circularly polarized pulses in a broad range of plasma electron densities from $n_e \simeq 1.7 \times 10^{19}$ to $7 \times 10^{19} \text{ cm}^{-3}$. The harmonic base frequency ω_f is downshifted from the laser frequency ω_0 , Fig. 2(b,c), in correlation with the transmitted laser spectra.

The data obtained with different lasers demonstrate the effect’s reproducibility and robustness and the photon yield scalability with the laser power, Fig. 2(c). For the 120 TW laser, the photon number and energy in unit solid angle within one harmonic at 120 eV are 2×10^{12}

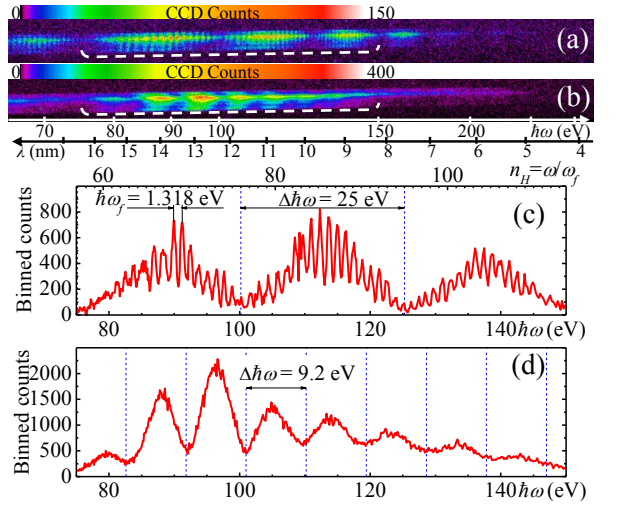


FIG. 3. (Color) Modulated spectra with (a) resolved and (b) nearly unresolved harmonic structure for $P_0 = 9$ TW, $n_e = 4.7 \times 10^{19} \text{ cm}^{-3}$. Line-outs (c) and (d) show spectra denoted by dashed brackets in (a) and (b), respectively.

photons/sr and $40 \mu\text{J}/\text{sr}$, respectively. These amount to 4×10^9 photons and 90 nJ, assuming 1.5° angular radius inferred from our particle-in-cell (PIC) simulations, which agrees with similar spectral intensities observed at 0 and 0.53° channels. Fig. 2(d) shows the spectrum up to the spectrograph throughput cut-off of 360 eV. The emission reaches the ‘water window’ region (284-543 eV), required for high-contrast femtosecond bioimaging, where the 9 TW laser produces $(1.5^{+0.6}_{-0.4}) \times 10^{10}$ photons/sr and $0.8^{+0.3}_{-0.2} \mu\text{J}/\text{sr}$, corresponding to 3×10^7 photons and 1.7 nJ for the same 1.5° radius. The uncertainties are due to the 10% filter thickness tolerance and CCD noise.

A large number of resolved harmonics, e. g. $n_H^* \simeq 126$ in Fig. 2(a,b) and $\gtrsim 160$ in Fig. 2(c, inset), strictly bounds the laser frequency change during the harmonic emission process, $\delta\omega/\omega \leq 1/(2n_H^*)$, otherwise the orders n_H^* and $n_H^* + 1$ overlap. The laser frequency decreases due to an adiabatic depletion of the laser pulse losing energy on plasma waves, while the number of photons is conserved [17–19]. For slow depletion, the frequency downshift rate equals the energy depletion rate, $\delta\omega/\omega = -\delta x/L_{\text{dep}}$ [17–19]. For Fig. 2(a,b), the depletion length is $L_{\text{dep}} \approx 2.7 \text{ mm}$ estimated from the observed 70% energy transmission through the 0.9 mm plasma. Estimate [19] gives a similar value, $L_{\text{dep}} \approx 8.7(n_{\text{cr}}/n_e)^{3/2}\lambda \approx 3.4 \text{ mm}$. The condition $\delta\omega/\omega < 0.4\%$ (or, alternatively, the phase error of $< 25 \text{ mrad}$) gives the harmonic emission length of $\lesssim 12 \mu\text{m}$. We note that the emission length can be much longer than the longitudinal size of the moving source.

In many shots with linear polarization (40% with the 9 TW laser), the harmonic spectrum exhibits deep equidistant modulations, Fig. 3. They are visible with discernible high orders and even with nearly unresolved individual harmonics in some shots, Fig. 3(b,d), where blur-

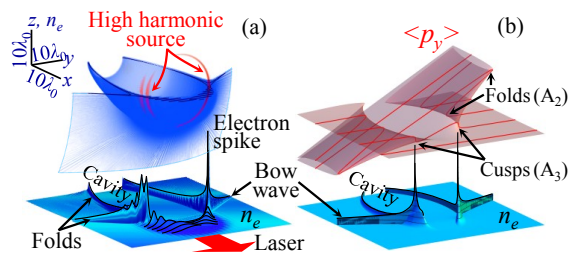


FIG. 4. (Color) (a) 3D PIC simulation. Electron density n_e (top, upper half removed) and its cross-section at $z = 0$ (bottom). The electromagnetic energy density for $\omega \geq 4\omega_0$ (red arcs). (b) Catastrophe theory model. Singularities in the electron density created by foldings of the electron phase space $(x, y, \langle p_y \rangle)$, where p_y is averaged over the laser period.

ring can be caused by a greater downshift of the laser frequency during a longer emission of harmonics, consistently exhibiting a few times greater photon number. Since in some cases the modulation depth is $\sim 100\%$, we conclude that the modulations result from interference between two almost identical strongly localized coherent sources separated in time and/or space. In shots with circularly polarized pulses (90 shots with the 120 TW laser), large-scale spectral modulations are not observed.

The unique properties of the observed harmonics mismatch previously suggested mechanisms of high-order harmonics generation. Atomic harmonics are excluded because both linearly and circularly polarized laser pulses produce both even and odd harmonic orders with a weak sensitivity to gas pressure. Betatron radiation is not relevant because the base frequency of its harmonics is determined by the plasma frequency and electron energy, not the laser frequency. Nonlinear Thomson scattering cannot provide the observed photon numbers even under the most favorable assumptions. For the 9 TW shot, Fig. 2(a,b,c), the numerical calculation of single-electron radiation spectra [7, 20] gives at 100 eV at most 2×10^{-10} nJ/eV sr, assuming the self-focused laser amplitude of $a_0 = 7$, pulse duration of 30 fs, and the observation angle of 15° close to optimum [7], where the high-frequency nonlinear Thomson scattering component is most intense. The number of electrons encountered by the laser pulse is $N_e = \pi d_{sf}^2 \Delta x n_e / 4 \approx 6 \times 10^9$, where $n_e = 2.7 \times 10^{19} \text{cm}^{-3}$, $d_{sf} \approx 5 \mu\text{m}$ is the self-focusing channel diameter [21], and $\Delta x \approx 12 \mu\text{m}$ is the harmonics emission length (see above). This gives at most 1 nJ/eV·sr, 200 times smaller than experimentally observed. For other spectra shown in Fig. 2(c,d) even less fraction corresponds to nonlinear Thomson scattering.

We performed two- (2D) and three-dimensional (3D) PIC simulations of harmonics generation using the code REMP [22]. As seen in simulations [23, 24], the laser pulse undergoes self-focusing [2, 18], pushes electrons out evacuating a cavity in electron density [18, 25] and generating a bow wave [26]. Fig. 4(a) represents the case

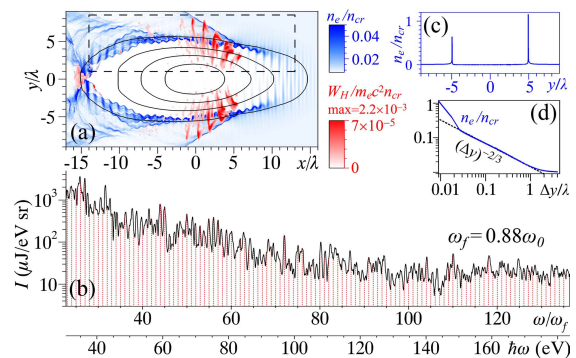


FIG. 5. (Color) 2D PIC simulation. (a) The electron density (blue), laser envelope (curves for $a = 1, 4, 7, 10$), and electromagnetic energy density, W_H , for frequencies from 60 to $100\omega_0$ (red). (b) The upper spike emission spectrum for the dashed rectangle in (a). (c) The electron density profile 10 laser cycles earlier than (a) and the right spike structure (d).

when a linearly polarized (along y axis) laser pulse self-focused to the amplitude of $a_0 = 6.6$ and FWHM waist of $10\lambda_0$, reaches a point where $n_e = 1.8 \times 10^{18} \text{cm}^{-3}$. The simulation window size is $125\lambda_0 \times 124\lambda_0 \times 124\lambda_0$ with the resolution of $dx = \lambda/32$, $dy = dz = \lambda/8$; the number of quasi-particles is 2.3×10^{10} ; ions are immobile. The electromagnetic energy density of a high-frequency ($\omega \geq 4\omega_0$) field reveals the source of high-order harmonics, Fig. 4(a, red arcs): they are emitted by the oscillating electron density spikes formed at the joining of the bow wave and cavity boundaries. While emission is also seen from the cavity walls [12], at higher frequencies such stronger radiation originates from the electron spikes.

The high-order harmonics emitted by the electron spikes are seen in 2D PIC simulation, performed in the $87\lambda_0 \times 72\lambda_0$ window with $dx = \lambda_0/1024$, $dy = \lambda_0/112$ and 6×10^8 quasi-particles. In Fig. 5, the laser pulse acquiring the amplitude of $a_0 = 10$, the duration of $16\lambda_0$ and the waist of $10\lambda_0$ meets plasma with $n_e = 1.7 \times 10^{19} \text{cm}^{-3}$. Starting from the 7th order, harmonics are well discernible up to the 128th order, as allowed by the simulation resolution. The emission is slightly off-axis with the angle decreasing with increasing harmonic order.

A strong localization of electron spikes, their robustness to oscillations imposed by the laser and, ultimately, their superior contribution to high-order harmonics emission is explained by catastrophe theory [27]. The laser pulse creates a multi-stream electron flow [28, 29] stretching and folding an initially flat surface formed by electrons in their phase space, Fig. 4(b), [23, 30]. The surface projection onto the (x, y) plane gives the electron density where outer and inner folds are mapped into singular curves outlining the bow wave and cavity boundaries, respectively. Catastrophe theory here establishes universal structurally stable singularities, insensitive to perturbations. The bow wave and cavity boundaries produce the

‘fold’ type singularity (A_2 , according to Arnold’s classification [27]), where the density grows as $(\Delta y)^{-1/2}$ with decreasing distance to the boundary, Δy . At the joint of the two folds, the density grows as $(\Delta y)^{-2/3}$, forming a higher order singularity – the ‘cusp’ (A_3), Fig. 5(c,d), [23, 31]. Stronger singularities exist [29], however they are not stable against perturbations. Located in a ring surrounding the cavity head, the cusp is seen in simulations as an electron spike. For linear polarization, the harmonic emitting ring breaks up into two segments, Fig. 4(a). The spike oscillations imposed by the laser generate high-order harmonics. The cusp singularity ensures a tight concentration of electric charge, making the emission coherent, i. e. the intensity is proportional to the particle number squared N_e^2 , similarly to the coherent nonlinear Thomson scattering. However, the cusp consists of different particles at every moment of time, in contrast to a synchronous motion of the same particles. We note that for constructive interference it is sufficient that the source size is smaller than the emitted wavelength in the direction of observation only. The estimated number of electrons within the singularity ring, $N_e \sim 10^6$, provides a signal level close to the experiment.

In classical electrodynamics [20], an oscillating electron emits harmonics up to critical order n_{Hc} , proportional to the cube of the particle energy $\mathcal{E}_e \approx a_0 m c^2$,

$$n_{Hc} = \omega_c / \omega_f \sim a_0^3, \quad (1)$$

then the spectrum exponentially vanishes as seen in our experiments. This gives clues about the harmonics generation scaling. For the laser dimensionless amplitude in the stationary self-focusing [21], $a_{0, sf} = (8\pi P_0 n_e / P_c n_{cr})^{1/3}$, we obtain the critical harmonic order of $n_{Hc} \sim P_0 n_e / P_c n_{cr}$, where $P_c = 2m_e^2 c^5 / e^2 \approx 17$ GW. The total energy \mathcal{E}_s emitted by the electron spike [20] is proportional to N_e^2 and the harmonic emission time τ_H :

$$\mathcal{E}_s \approx e^2 N_e^2 a_0^4 \gamma \omega_0^2 \tau_H / 8c \propto N_e^2 P_0^{4/3} n_e^{5/6} \omega_0^{1/3} \tau_H. \quad (2)$$

Here $\gamma \approx (n_{cr} / n_e)^{1/2}$ is the Lorentz factor associated with the spike velocity, which is close to the laser pulse group velocity in plasma. In the 120 TW shot, Fig. 2(c), the energy emitted into a harmonic near 120 eV is 40 μ J/sr. In the 2D PIC simulation with the parameters close to this shot (Fig. 5), the energy of 100th harmonic is 30 μ J/sr. An estimate based on Eq. (2) gives 100 μ J/sr within the 100th harmonic, thus providing a simple analytical estimate for the expected harmonic energy.

With the detector at 1.4 m and the source size of 10 μ m estimated from simulations, the spatial coherence width is 1 mm, which is large enough for many phase contrast imaging applications in a compact setup [32].

In conclusion, irradiating gas jets with multi-terawatt lasers we observe comb-like harmonic spectra reaching the ‘water window’ region. We propose the harmonic generation mechanism based on self-focusing, nonlinear

wave formation with electron density spikes, and collective radiation by a compact electric charge. Catastrophe theory explains the electron spike sharpness and stability. The maximum harmonic order scaling with the laser intensity will allow reaching the keV range. Our results open the way to a compact coherent X-ray source built on a university laboratory scale repetitive laser and accessible, replenishable and debris-free gas jet target. This will impact many areas requiring a bright X-ray/XUV source for pumping, probing, imaging, or attosecond science.

We acknowledge the financial support from MEXT (Kakenhi 20244065, 21604008, 21740302, and 23740413), JAEA President Grant, and STFC facility access fund.

-
- [1] U. Teubner and P. Gibbon, *Rev. Mod. Phys.* **81**, 445 (2009).
 - [2] G. A. Mourou *et al.*, *Rev. Mod. Phys.* **78**, 309 (2006).
 - [3] A. McPherson *et al.*, *J. Opt. Soc. Am. B* **4**, 595 (1987); P. B. Corkum, *Phys. Rev. Lett.* **71**, 1994 (1993); F. Krausz and M. Ivanov, *Rev. Mod. Phys.* **81**, 163 (2009).
 - [4] D. L. Matthews *et al.*, *Phys. Rev. Lett.* **54**, 110 (1985); S. Suckewer *et al.*, *ibid.* **55**, 1753 (1985); H. Daido, *Rep. Prog. Phys.* **65**, 1513 (2002).
 - [5] E. Esarey *et al.*, *Phys. Rev. E* **48**, 3003 (1993).
 - [6] S. Y. Chen *et al.*, *Nature* **396**, 653 (1998); *Phys. Rev. Lett.* **84**, 5528 (2000); K. Ta Phuoc *et al.*, **91**, 195001 (2003); S. Banerjee *et al.*, *J. Opt. Soc. Am. B* **20**, 182 (2003).
 - [7] K. Lee *et al.*, *Phys. Rev. E* **67**, 026502 (2003).
 - [8] R. W. Schoenlein *et al.*, *Science* **274**, 236 (1996); M. Babzien *et al.*, *Phys. Rev. Lett.* **96**, 054802 (2006).
 - [9] F. Albert *et al.*, *Plasma Phys. Control. Fusion* **50**, 124008 (2008); S. Kneip *et al.*, *Nature Phys.* **6**, 980 (2010).
 - [10] S. V. Bulanov *et al.*, *Phys. Rev. Lett.* **91**, 085001 (2003); M. Kando *et al.*, **99**, 135001 (2007); **103**, 235003 (2009); A. S. Pirozhkov *et al.*, *Phys. Plasmas* **14**, 123106 (2007).
 - [11] S. V. Bulanov *et al.*, *Phys. Plasmas* **1**, 745 (1994); B. Dromey *et al.*, *Nature Phys.* **2**, 456 (2006); C. Thaury *et al.*, **3**, 424 (2007); Y. Nomura *et al.*, **5**, 124 (2009).
 - [12] D. F. Gordon *et al.*, *Phys. Rev. Lett.* **101**, 045004 (2008).
 - [13] H. Kiriya *et al.*, *Opt. Lett.* **33**, 645 (2008).
 - [14] C. J. Hooker *et al.*, *J. de Phys. IV* **133**, 673 (2006).
 - [15] I. W. Choi *et al.*, *Appl. Opt.* **36**, 1457 (1997); D. Neely *et al.*, *AIP Conf. Proc.* **426**, 479 (1998).
 - [16] B. L. Henke *et al.*, *At. Data Nucl. Data Tables* **54**, 181 (1993), http://henke.lbl.gov/optical_constants/.
 - [17] S. V. Bulanov *et al.*, *Phys. Fluids B* **4**, 1935 (1992).
 - [18] E. Esarey *et al.*, *Rev. Mod. Phys.* **81**, 1229 (2009).
 - [19] B. A. Shadwick *et al.*, *Phys. Plasmas* **16**, 056704 (2009).
 - [20] J. D. Jackson, *Classical Electrodynamics*, 3rd ed. (John Wiley & Sons, New York, 1998).
 - [21] S. S. Bulanov *et al.*, *Phys. Plasmas* **17**, 043105 (2010).
 - [22] T. Z. Esirkepov, *Comput. Phys. Comm.* **135**, 144 (2001).
 - [23] Supplemental Material at [URL].
 - [24] Supplemental Movie S1 at [URL].
 - [25] A. Pukhov and J. Meyer-ter Vehn, *Appl. Phys. B* **74**, 355 (2002).
 - [26] T. Z. Esirkepov *et al.*, *Phys. Rev. Lett.* **101**, 265001

- (2008).
- [27] T. Poston and I. Stewart, *Catastrophe theory and its applications* (Dover, 1996).
- [28] S. V. Bulanov *et al.*, Phys. Rev. Lett. **78**, 4205 (1997).
- [29] A. V. Panchenko *et al.*, Phys. Rev. E **78**, 056402 (2008).
- [30] Supplemental Movie S2 at [URL].
- [31] Supplemental Movie S3 at [URL].
- [32] S. W. Wilkins *et al.*, Nature **384**, 335 (1996); H. N. Chapman and K. A. Nugent, Nat. Photon **4**, 833 (2010); B. Abbey *et al.*, **5**, 420 (2011).